Research Article Vol. 31, No. 2 / 16 Jan 2023 / Optics Express 2480
Optics EXPRESS

# Simultaneously improving the quality factor and outcoupling efficiency of organic light-emitting field-effect transistors with planar microcavity

QIAOXIA GONG,[1] WENBO ZHANG,[1] JIURU HE,[1] FENGYING MA,[1] LI SONG,[2] LIWEN CHENG,[3] JUN ZHANG,[4,5] LIJUN WANG,[4] AND YONGSHENG HU[1,*]

[1]School of Physics and Microelectronics, Key Laboratory of Materials Physics of Ministry of Education, Zhengzhou University, Zhengzhou 450001, China
[2]Tianjin Key Laboratory of Electronic Materials and Devices, School of Electronics and Information Engineering, Hebei University of Technology, Tianjin 300401, China
[3]College of Physical Science and Technology, Yangzhou University, Yangzhou 225002, China
[4]State Key Laboratory of Luminescence and Applications, Changchun Institute of Optics Fine Mechanics and Physics, Chinese Academy of Sciences, Changchun 130033, China
[5]jzh_ciomp@163.com
*huyongsheng@zzu.edu.cn

**Abstract:** Organic light-emitting field-effect transistors (OLEFETs) are regarded as an ideal device platform to achieve electrically pumped organic semiconductor lasers (OSLs). However, the incorporation of a high-quality resonator into OLEFETs is still challenging since the process usually induces irreparable deterioration to the electric-related emission performance of the device. We here propose a dual distributed Bragg reflector (DBR)-based planar microcavity, which is verified to be highly compatible with the OLEFETs. The dual DBR planar microcavity shows the great advantage of simultaneously promoting the quality (Q) factor and outcoupling efficiency of the device due to the reduced optical loss. As a result, a moderately high Q factor of ~160, corresponding to EL spectrum linewidth as narrow as 3.2 nm, concomitantly with high outcoupling efficiency (~7.1%) has been successfully obtained. Our results manifest that the dual DBR-based planar microcavity is a promising type of resonator, which might find potential applications in improving the spectra and efficiency performance of OLEFETs as well as in OLEFET-based electrically pumped OSLs.



## 1. Introduction

Organic light-emitting field-effect transistors (OLEFETs) have emerged as a kind of multifunctional device which combines the switching property of a transistor and the emitting property of an organic light-emitting device (OLED), showing great potential for use in simplified displays, integrated optical communication, and even electrically pumped organic semiconductor lasers (OSLs) [1,2]. When used as a platform for electrically pumped OSLs, the OLEFETs have many advantages [3–5] e.g., (1) a higher carrier density (current density) due to the field-effect and a wider choice of organic semiconductors with higher mobility, thus better meeting the requirement of high laser threshold; (2) efficient light confinement due to the concentrated exciton recombination zone; (3) possibly minimized excitonic losses due to the separation between the excitons and the carriers and electrodes. With the great efforts during the past decade, the external quantum efficiency (EQE) for this kind of device has reached ~20% which is now comparable with two terminal light-emitting devices (LEDs) such as organic and colloidal quantum dots-based LEDs [6,7]. However, the challenge of building a suitable resonator to provide effective optical feedback and mode selection in OLEFETs without sacrificing their

#479422 https://doi.org/10.1364/OE.479422
Journal © 2023 Received 27 Oct 2022; revised 13 Dec 2022; accepted 20 Dec 2022; published 10 Jan 2023

Optics EXPRESS

electroluminescence (EL) performance such as EQE and current density, which is a prerequisite for achieving OLEFET-based lasers, still exists.

Resonators such as F-P cavity, distributed feedback (DFB) cavity, and 1D/2D photonic crystal have been widely investigated in OLEFETs due to their relatively facile fabrication processes [8–10]. Among them, the F-P cavity is based on the natural cleavage plane of organic crystals, while the cleavage plane is not usually as regular as the inorganic crystals due to the weak van der Waals force. Besides, the reflectance at the cleavage plane is not adequately high which may induce large optical loss [3,11]. For the DFB cavity, despite the mature technology of micro-nano fabrication, it is still challenging to guarantee both high optical and electrical performance due to the incompatible process between the organic semiconductors and traditional micro-nano fabrication technologies (e.g. photolithography). Consequently, although narrow EL spectra linewidth (full width at half maxima (FWHM) of several nanometers) have been observed in these devices, the EQE of the devices are quite low, which are mainly limited by their low outcoupling efficiency and exciton recombination efficiency [12,13]. This will bring great barriers for future laser devices since it inevitably increases the threshold current density and decreases the slope efficiency.

Planar microcavity consists of two closely parallel mirrors is another prevailing type of resonator which have been widely used in vertical cavity surface-emitting lasers based on both III-V semiconductors and solution-processed semiconductors, including organic materials [14–16]. It is generally believed that a high Q factor facilitates a low lasing threshold owing to a reduced optical loss and enhanced spontaneous emission factor [17]. However, so far, the planar microcavity reported in OLEFETs has been mainly used to improve the EQE of the devices by taking advantage of the Purcell effect [18,19]. In this case, a relatively low quality (Q) factor is usually required to make full use of the photons with different energies to guarantee an overall high EQE [6,20]. In the previous work, we attempted to improve the Q factor by using a highly reflective distributed Bragg reflector (DBRs) combined with an Ag electrode as the other mirror in the OLEFETs; however, restricted by the absorption loss of the Ag electrode, the Q factor of the device was limited to lower than 90 [21].

In this work, we focus on planar microcavity OLEFETs with dual DBR to simultaneously improve the Q factor and outcoupling efficiency of the device. At first, the influence of the cavity structure, including the DBR, electrode, and dielectric layer, is systematically investigated through simulation. Thereafter, we fabricate the first planar microcavity OLEFETs with dual DBR, which exhibits a moderately high Q factor of ~160. The EL spectrum linewidth as narrow as 3.2 nm concomitantly with a high outcoupling efficiency of ~7.1% have been successfully obtained. Our results provide a viable route towards building a high-quality resonator that is compatible with OLEFETs, which might find potential applications in improving the spectra and efficiency performance of OLEFETs as well as in OLEFET-based electrically pumped OSLs.

## 2. Result and discussion

### 2.1. Basic structure of dual DBR-based planar microcavity OLEFETs

Figure 1(a) presents a simplified optical schematic of the devices. Photons are generated from the radiation recombination of excitons in the emission layer, and resonated between the bottom and top DBR to form a standing wave field in the cavity. The light emission is collected from the top DBR due to the lower reflectance compared to the bottom DBR. Figure 1(b) shows the schematic of the planar microcavity OLEFETs, where the OLEFET is sandwiched between a bottom and a top DBR. The OLEFETs have a similar structure as we reported previously [22] with the ITO acting as the gate electrode, poly-4-vinylphenol (PVP)/polystyrene (PS) acting as the dielectric layer, pentacene/NPB/HAT-CN/ CBP:Ir(ppy)$_3$/Bphen/Bphen:Cs acting as the organic active layers, and a thin layer of Ag acting as the source/drain (S/D) electrodes. Here, the pentacene/NPB/HAT-CN, CBP:Ir(ppy)$_3$, and Bphen/Bphen:Cs are the hole transport layer,

Optics EXPRESS

emission layer and electron transport layer, respectively. The planar microcavity is comprised by a bottom and a top DBR, which was comprised of a few pairs of $TiO_2/SiO_2$ and $ZnS/MgF_2$ quarter-wave layers, respectively.

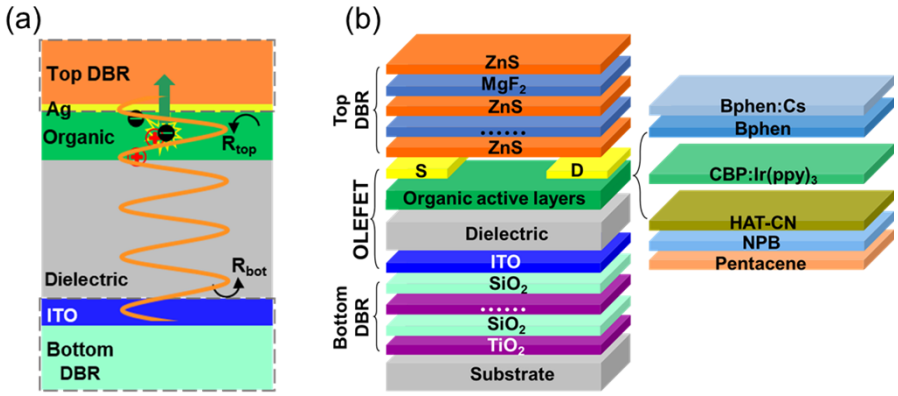


**Fig. 1.** (a) A simplified two-dimensional optical schematic that is used to simulate the field distribution of the device. (b) Schematic of the microcavity OLEFET, which is consisted by the bottom DBR, OLEFET and top DBR.

### *2.2. Optical design of planar microcavity OLEFETs*

The application of microcavity structure in OLEFET is investigated using optical modeling. We first investigate the influence of the cavity structure on the key optical characteristics including the Q factor and outcoupling efficiency of the device. Since the structure and fabrication of the bottom DBR and ITO are quite mature and have been investigated previously [21,23], we will fix them to 15 pairs and 86 nm, respectively, which represents a high reflectance of ~97.9% in the wavelength range of 450~590 nm (not given). Alternatively, we here focus on the top DBR, Ag electrode, and dielectric layer since they are the leading factors that directly determine the resonance properties of the resonator.

Figure 2(a) shows the influence of the top DBR on the Q factor and outcoupling efficiency of the device. As the number of pairs of $ZnS/MgF_2$ increases from 2.5 to 8.5, the Q factor increases continuously, and then turns saturation as the number of pairs gets beyond. This can be ascribed to the change of the reflectance of the top DBR since the Q factor is closely related to the reflectance of the mirrors by [24],

$$Q = \frac{\lambda}{\Delta\lambda} = \frac{2\pi n L_{cav}}{\lambda} \frac{1}{\alpha L_{cav} - \ln(\sqrt{R_{top-}R_{bot}})}, \tag{1}$$

where $\Delta\lambda$ is FWHM, $L_{cav}$ and n are the effective cavity length and the effective refractive index, respectively, $\alpha$ is an average distributed loss constant; $R_{bot}$ and $R_{top}$ are the reflectance of the bottom mirror and the top mirror, respectively. While the reflectance of the DBR is determined by its number of pairs as described by [25],

$$R = \left( \frac{n_0 (n_L)^{2N} - n_S (n_H)^{2N}}{n_0 (n_L)^{2N} + n_S (n_H)^{2N}} \right)^2, \tag{2}$$

where N is the number of pairs of layers in the stack, and $n_0$, $n_H$, $n_L$, and $n_S$ are the refractive index of the medium (in this case: air), the high and low index materials, and the substrate, respectively.

Optics EXPRESS

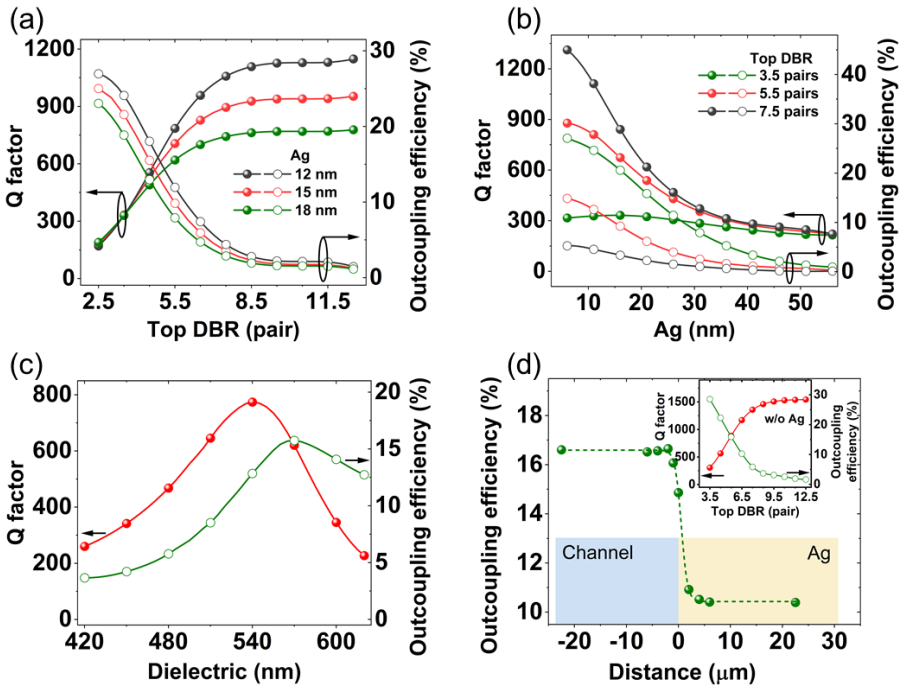


**Fig. 2.** Optical design of the proposed microcavity OLEFET. Influence of (a) top DBR and (b) Ag electrode on device performance (Q factor and outcoupling efficiency). (c) Influence of the thickness of dielectric layer on Q factor and outcoupling efficiency (top DBR of 5.5 pairs and Ag of 15 nm). (d) Outcoupling efficiency for emission at different areas (top DBR of 5.5 pairs and dielectric of 520 nm). Inset: Q factor and outcoupling efficiency for emission in the channel.

Figure 2(a) also shows that the thinner the Ag is, the higher the upper limit of Q factor will be. This is because that Ag exhibits strong absorption in the visible light range, thereby a thicker Ag would induce more absorption loss. The maximum Q factor reaches ~1100 for the case of 12 nm Ag. Comparatively, the outcoupling efficiency exhibits an opposite tendency which decreases from ~25% to ~ 1.8% as the pair of DBR increases, while a thicker Ag leads to a lower outcoupling efficiency. This is reasonable when considering the reduced transmittance as the pair of DBR and thickness of Ag increase.

The influence of the thickness of Ag can be seen more clearly in Fig. 2(b). As Ag increases (e.g. from 6 nm to 56 nm), both the Q factor and the outcoupling efficiency decrease drastically, especially for device with more pairs of DBR (e.g. 5.5 and 7.5 pairs). Again, larger pairs of DBR renders higher Q factor. These results suggest that an Ag electrode as thin as possible, combined with a top DBR with a certain large number of pair are preferred for the OLEFETs. Considering the process complexity of the top DBR, and the minimum thickness requirement for the conductivity of the S/D electrodes, we use 5.5 pairs and 15 nm for top DBR and Ag, respectively, in later experiment.

Since the thickness of dielectric would influence the distribution of the standing wave electric field, the Q factor and outcoupling efficiency should be affected accordingly. As is shown in Fig. 2(c), as the dielectric changes from 420 nm to 620 nm, a maximum Q factor of ~770 appears around 540 nm. The corresponding outcoupling efficiency is ~12.8%. The outcoupling efficiency remains above 10% in a wide range of thickness from 525 nm to 620 nm, which indicates a favorably high tolerance for the thickness of dielectric.

Optics EXPRESS

In the above discussion, the emission (exciton recombination) area is located beneath the drain electrode since the OLEFETs in this work are unipolar [22] which will be discussed later. However, it is possible to tune the emission area into the channel if the balance between the holes and electrons is improved, as has been widely reported in ambipolar OLEFETs [26–28]. In this case, the adverse effects from Ag can be completely eliminated. Figure 2(d) shows the simulated results where the outcoupling efficiency improves substantially by ~60% from 10.5% to 16.5%. Moreover, the corresponding Q factor further increases from ~700 to ~880 for the case of 5.5 pairs of top DBR, and a maximum of more than 1500 could even be obtained (inset of Fig. 2(d)). These results highlight the superiority of ambipolar OLEFETs in building planar microcavity devices, which might be an appealing option of device architecture in the future.

### 2.3. Performance of fabricated dual DBR-based planar microcavity OLEFETs

Based on the above simulation, we fabricated the dual DBR-based planar microcavity OLEFETs with a top DBR with 5.5 pairs of ZnS/$MgF_2$, 15 nm Ag, and 540 nm dielectric layer. Figure 3(a) shows the cross sectional scanning electron microscope (SEM) image of the device. The bottom DBR (partially given for better showing the upper part) and ITO can be clearly distinguished as compact and smooth layers. It should be mentioned that traditional fabrication techniques of DBR, such as sputtering and high temperature e-beam evaporation, usually lead to irreparable deterioration to the device when fabricated on top of soft materials such as organic semiconductors, colloidal quantum dots, and perovskites. Therefore, it is actually very challenging to incorporate a high quality top DBR into the device, especially under the case of electrical injection [14,29]. The top DBR (5.5 pairs) here was fabricated by e-beam evaporation at room temperature (Fig. 3(c)) to avoid inducing damage on the underlying organic active layers. The top DBR is less compact compared to the bottom DBR; however, given to the atomic force microscope (AFM) images in Fig. 3(b), it exhibits a low surface roughness with root-mean-square (RMS) of only 1.8 nm, representing a smooth morphology comparable to those in the literature [14].

The top DBR also shows good optical performance as shown in Fig. 3(d) where the reflectance and transmittance spectra of the top composite mirror (5.5 pairs DBR + 15 nm Ag) are given. For better comparison, the results for Ag-only mirror (80 nm) are also presented. The reflectance around the central wavelength of 515 nm is about 96.9% for the composite mirror, which is already beyond that of Ag-only mirror (96.3%). The reflectance could be further improved by increasing the number of pairs of the ZnS/$MgF_2$. Meanwhile, the absorption (100%-R-T, R and T are the reflectance and the transmittance, respectively) near the central wavelength for the composite mirror is reduced to 2.7% compared to 3.65% for Ag-only mirror. This reduction can further facilitate the increase of both the Q factor and the EQE of the device.

We next investigate the optical characteristics of the whole device. The reflectance spectrum of the device (Fig. 4(a)) shows a wide stopband between 460 nm and 590 nm with a clear resonated dip at 526 nm. The resonated dip is well located near the peak of the EL spectrum without cavity (Fig. 4(a)), indicating a reasonable configuration of the cavity. The device shows a sharp emission peak at 526 nm and several weak emission peaks (e.g. 585 nm, 629 nm) at longer wavelength range. We speculate that these peaks are the resonant modes of the microcavity since they agree well with the transmission bands in the reflectance spectrum (Fig. 4(a)). Notably, the FWHM linewidth of the peak at 526 nm is only 3.2 nm, indicating a Q factor of ~160 which is much higher than that with planar microcavity comprised of DBR and thick Ag [21]. The Q factor is lower than the simulated result, which is probably due to extra optical loss resulting from either the residual material absorption or nonideal fabrication process. In spite of this, to the best of our knowledge, it is still among the best for OLEFETs with other types of the resonator, especially those with planar microcavity reported to date. Table 1 summarizes some representative OLEDs and OLEFETs with narrow emission linewidth. For the OLEDs, both DBR with thick metal mirrors and dual DBR has been demonstrated, which exhibit both narrow

Optics EXPRESS

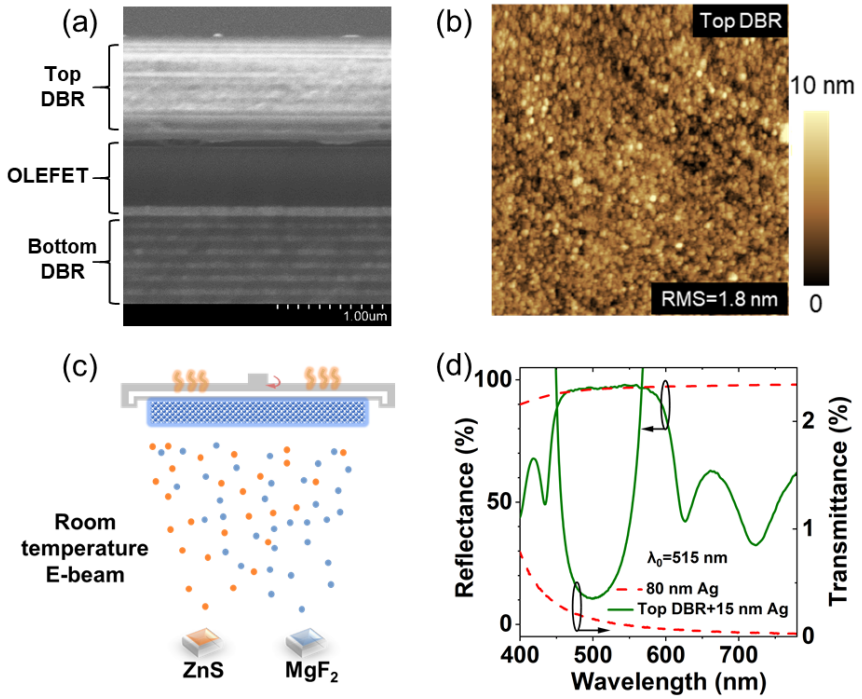


**Fig. 3.** Fabrication and characterization of top DBR. (a) Cross sectional SEM image of the device. (b) AFM topography (5 μm × 5 μm) of top DBR (the top surface of the entire device). (c) Schematic of the room temperature e-beam evaporation for fabrication of top DBR. (d) Reflectance and transmittance spectra for 80 nm Ag and the top mirror.

linewidth and appreciable EQE. Ref. 31 even shows higher EQE than that of the OLEFETs in this work; however, a main barrier for the OLEDs is their much lower level of current density which is usually far below the requirement of electrically pumped OSLs [33–35]. Meanwhile, the electrode absorption in the OLEDs could not be neglected or eliminated as what might happen in ambipolar OLEFETs (Fig. 2(d)). It is worth mentioning that by using other methods such as adopting a sacrificing layer, one can also obtain high quality microcavity with dual DBR [32], however, this usually causes nonnegligible decrease to the electrical and related optical performance of the device with relatively low EQE [32]. While for the OLEFETs, the incorporation of cavities such as F-P and DFB also leads to extremely low EQE [3,12,13] mainly due to their incompatible fabrication process as discussed before. Therefore, the planar microcavity with dual DBR in this work shows apparent advantage in achieving both narrow emission linewidth and high EQE.

Figure 4(b) shows a 2D pseudo-color plot of the EL spectra as a function of the viewing angle, where four transmitted modes centered at 526 nm, 585 nm, 629 nm, and 654 nm, respectively, can be clearly observed. The resonated mode at 526 nm blue shifts as the viewing angle increases from 0° to 40°. This is a typical characteristic for planar microcavity devices which is determined by the resonance condition [36]: $2dn\cos\psi=m\lambda$, where d is the geometric cavity length, n is the average refractive index of the layers between the mirrors, ψ is the emission angle inside the cavity, and m is the mode number in integer form. The modes at 585 nm, 629 nm, and 654 nm also exhibit a blue-shift under small viewing angles (<25°). For large viewing angles, continuous spectra bands appear in these modes, which can be ascribed to the blue-shift of the high reflectance band according to the Bragg's law [37], leading to the superposition of weak resonant modes and non-resonant modes.

Optics EXPRESS

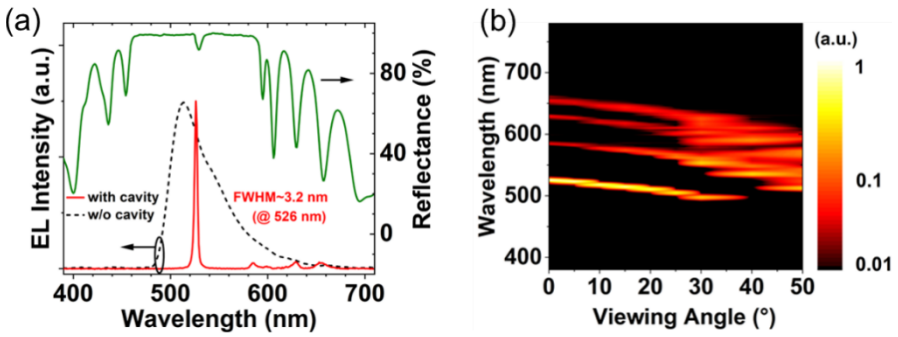


**Fig. 4.** Optical characteristics of the device. (a) EL spectra for devices with and without microcavity; reflectance spectrum for the entire device with microcavity (measured from the top side). (b) 2D pseudo-color plot of the EL spectra as a function of the viewing angle.

**Table 1. Comparison of narrow emissive (FWHM < 15 nm) OLEFETs and OLEDs with different resonators in literature**

| Device Type | Resonator Type | Emission Wavelength (nm) | FWHM (nm) | Q Factor | EQE at Maximal EL Intensity (%) | Ref. |
|---|---|---|---|---|---|---|
| OLED | DBR/Al | 462 | 2 | 231 | 1.72 | 23 |
| | DBR/Al | 393 | 10 | 39 | 4.31 | 30 |
| | Dual DBR | 564 | 6 | 94 | 0.92 | 31 |
| | Dual DBR | 555 | 2.7 | 206 | N/A | 32 |
| OLEFET | F-P | 616 | 14 | 44 | N/A | 3 |
| | 2D DFB | 555 | 9.8 | 57 | N/A | 12 |
| | DFB | 556 | 2.05 | 271 | $4.9\times10^{-5}$ | 13 |
| | DBR/Ag | 612 | 6.9 | 89 | 0.07 | 21 |
| | Dual DBR | 526 | 3.2 | 160 | 0.78 | This work |

We next discuss the electrical and related optical performance of the device. Figure 5(a) presents the electrical and optical transfer curves of the device at drain to source voltage $V_{DS}$ = -80 V. The drain current ($I_{DS}$) increases continually with the increase of gate to source voltages ($V_{GS}$) in the negative voltage range with ON/OFF ratio >$10^4$. The emission intensity (photocurrent) grows with the increase of the drain current. The output curves (Fig. 5(b)) under negative $V_{GS}$ from 0 V to -100 V show distinct linear and saturation regions, indicating a typical p-type characteristic. The hole mobility calculated in the saturation regime is 0.16 $cm^2V^{-1}s^{-1}$, which is close to that for devices without microcavity [22], confirming that the incorporation of a top DBR in this work brings negligible degradation to the electrical performance.

Figure 5(c) presents the EQE and current efficiency for the device. The maximum EQE and current efficiency reaches 0.78% and 3.2 $cdA^{-1}$, and maintains at ~0.5% and ~2 $cdA^{-1}$ at high drain current, respectively. These values are more than 10 times higher than those with planar microcavity comprises of DBR and thick Ag [21] (see Table 1). We assume that in addition to the higher exciton utilization efficiency of the phosphorescent emitter, this improvement can also be ascribed to the improved outcoupling efficiency. The outcoupling efficiency of the device can be estimated from: $EQE=\Phi_{capture}\Phi_{spin}\Phi_{PL}\Phi_{out}$, where $\Phi_{capture}$ is the recombination efficiency determined by the capture of electrons and holes injected into the emission layer (~12.5%) [22], $\Phi_{spin}$ is the exciton utilization efficiency (100%), $\Phi_{PL}$ is the PLQY of the emitter (88%), and $\Phi_{out}$

Optics EXPRESS

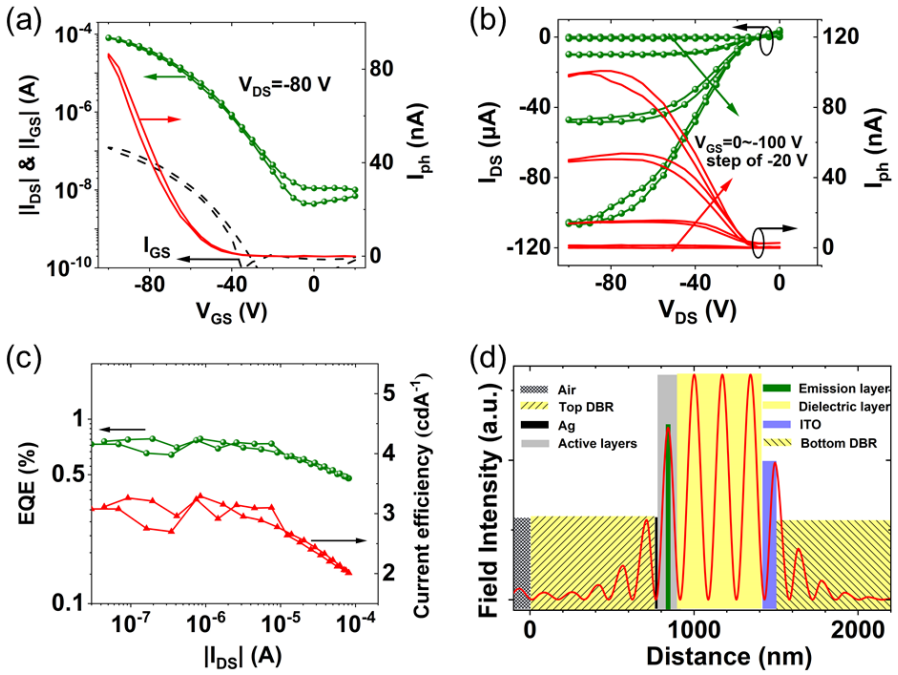


**Fig. 5.** Electrical characteristics of the device. (a) Transfer curves ($V_{DS}$ = -80 V). (b) output curves ($V_{GS}$ changes from 0 V to -100 V in step of -20 V). (c) EQE and current efficiency. (d) Simulated standing wave electric field distribution within the microcavity.

is the outcoupling efficiency, which could be derived to be ~7.1%. It is worth noting that the EQE of the device is appreciable high among OLEFETs with narrow (e.g. < 15 nm) EL spectrum (Table 1). In addition to the reduced absorption loss from thick Ag (Fig. 3(d)), we assume that the well-designed cavity also enables the high outcoupling efficiency, as could be seen from the simulated distribution of the standing wave electric field within the microcavity (Fig. 5(d)). There are 4 periodic standing waves between the electrodes of Ag and ITO, which corresponds to a 2λ cavity length. The emission layer overlaps well with the antinode near the Ag electrode (defines as the first standing wave), while Ag is located near the node of the first standing wave. This configuration is conducive to maximizing the photons from the emission layer and reducing the absorption loss from Ag electrode [38].

Figure 6 shows the top emission optical images of the device both with and without top DBR under different $V_{GS}$. The emission area for both devices is located beneath the drain electrode near the edge of the channel, which is consistent with the unipolar (p-type) characteristic of the devices. The width of emission area increases with the gate voltage for both cases. For the device with the top DBR (Fig. 6(a)-(c)), when the $V_{GS}$ increases from -60 V to -100 V, the width of the emission area increases from ~5 μm to ~50 μm. While for the device without the top DBR (Fig. 6(d)-(f)), it displays much brighter image intensity and thereby much larger emission width from ~25 μm to ~140 μm due to the increased outcoupling efficiency as the decrease of the number of pairs of top DBR (Fig. 2(a) and 2(b)).

We further investigated the EL spectra of the device under different injection levels. Figure 7(a) shows a 2D pseudo-color plot of the emission spectra as a function of the drain current. The four resonant modes centered at 526 nm, 585 nm, 629 nm, and 654 nm, respectively, can be clearly observed. These modes are quite stable as the drain current increases within the measured range (≤87 μA). The intensity of all these modes grows linearly with the drain current as shown in

Optics EXPRESS

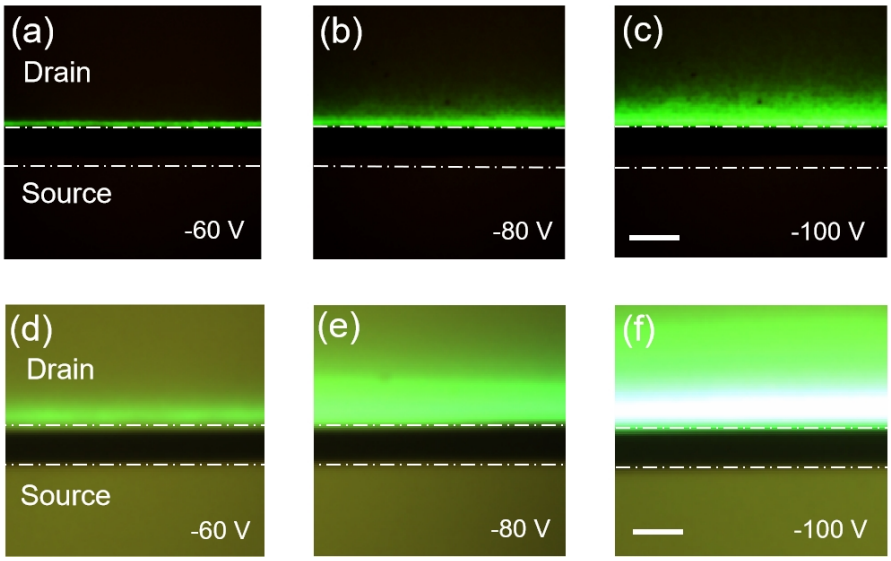


**Fig. 6.** Top emission optical images of the devices for (a)-(c) with and (d)-(f) without top DBR under the gate voltages of -60 V, -80 V, and -100 V, respectively. Scale bar is 60 μm.

Fig. 7(b) where two of the modes are selectively illustrated. Meanwhile, the FWHM linewidth of these modes remains stable to be 3.2 nm and 7.0 nm, respectively, for all the injection levels. These results indicate that there is no light amplification. This is reasonable since we use a traditional phosphorescent emitter in this work with the purpose of getting a high exciton utilization efficiency. It is generally believed that traditional phosphorescent emitters are not regarded as a good candidate for lasing due to their slow radiative transition and large optical loss from excited states [39,40]. Nevertheless, recently developed thermally activated delayed fluorescence (TADF) [41,42] and novel phosphorescent emitters [43,44] have shown the potential of light amplification, which might provide alternative route to lasing devices with comparable efficiency to traditional phosphorescent emitters.

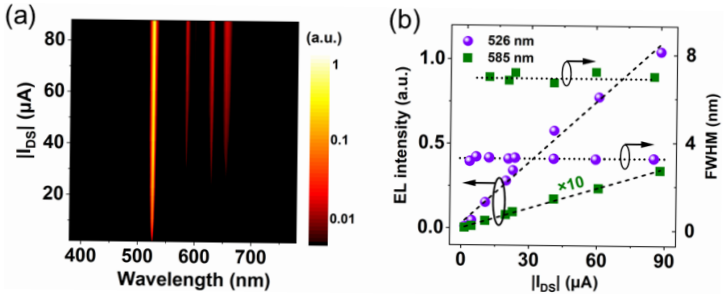


**Fig. 7.** (a) 2D pseudo-color plots of the EL spectra under different drain currents. (b) Intensity and FWHM of the emission peaks of 526 nm and 585 nm. The intensity for the peak of 585 nm is multiplied by 10 to allow easier comparison.

## 3. Conclusion

In conclusion, we have demonstrated that dual DBR planar microcavity is a type of resonator that is highly compatible with OLEFETs. It enables a simultaneous promotion of the Q

Optics EXPRESS

factor and outcoupling efficiency of the device compared to the lossy DBR/Ag microcavity. A moderately high Q factor (~160), corresponding to the EL spectrum linewidth as narrow as 3.2 nm, concomitantly with high outcoupling efficiency (~7.1%) have been successfully obtained. Our work might provide some insights into building high performance resonated OLEFETs, and pave the way towards OLEFET-based electrically pumped OSLs.

## 4. Experimental section

### 4.1. Device fabrication

$TiO_2$ (53.4 nm), $SiO_2$ (88.1 nm), and ITO (85 nm) were deposited onto the glass substrate by E-beam evaporation under a base pressure of $1.5 \times 10^{-4}$ Pa, evaporation rate of 2 Å/s, and substrate temperature of 300 °C. An end-Hall ion source was used to assist the deposition. ZnS (56 nm) and $MgF_2$ (93 nm) were deposited by E-beam evaporation under a base pressure of $1.5 \times 10^{-3}$ Pa, evaporation rate of 2 Å/s, and at room temperature. The thickness and evaporation rates were monitored by a quartz crystal microbalance positioned at the center of chamber. The PVP solution was prepared with poly(4-vinylphenol) and poly(melamine-co-formaldehyde) (2:1 wt%) dissolved in propylene glycol monomethyl ether acetate (PGMEA) (110 mg/mL). The PVP solution was spin-coated (30 s at 3000 rpm) and annealed at 200 °C for 1 h. The polystyrene (PS) dissolved in toluene (6 mg/mL) was successively spin coated (30 s at 3000 rpm) on PVP and annealed at 85 °C for 1 h. Pentacene (12 nm), NPB (10 nm), HAT-CN (2 nm), CBP:$Ir(ppy)_3$ (28 nm, 6 wt%), Bphen (9 nm) and Bphen:Cs (45 nm, 10 wt %) were successively thermal evaporated with the rate of 0.2, 0.2, 0.1, 2, 0.2 and 0.2 Å/s, respectively. Ag (15 nm) was evaporated through a shadow mask with channel length and width of 45 μm and 3000 μm, respectively. The thickness and evaporation rates of the organic materials as well as the electrodes were monitored by quartz-crystal oscillators and calibrated ex situ using a surface profiler (Ambios XP-1). The devices were encapsulated with epoxy resin in the glovebox ($H_2O$, $O_2 < 0.1$ ppm) before testing.

### 4.2. Device characterization

The electrical characteristics were performed by Keithley 4200 SCS at room temperature under air ambient. The photocurrent was recorded by HAMAMATSU S1336 photodiode. The optical images were captured by Olympus BX51TRF CCD microscope. The scanning electron microscopy (SEM) image was recorded by Hitachi SEM-S-4800. The atomic force microscopy (AFM) measurement was performed on Shimadzu SPM-9700. The reflectance and transmittance spectra were recorded by PerkinElmer Lambda 1050 UV-vis-NIR spectrophotometer. The carrier mobilities were calculated by the formula for the saturation regime: $I_{DS}=\mu C_i(W/2L)(V_{GS}-V_T)^2$, (where μ is the field-effect mobility, $C_i$ is the gate dielectric capacitance density, $V_T$ is the threshold voltage, W and L are the channel width and length, respectively). The EL spectra were measured by AvaSpec-ULS2048L fiber spectrometer. The EL spectra for different viewing angles were measured with a source meter (Keithley 2612B), goniometer and fiber spectrometer (AvaSpec-ULS2048L). The EQE was calculated from the brightness (photocurrent), the drain current, the EL spectra, and the angular distribution of EL intensity of the devices.

### 4.3. Optical simulation

Numerical simulations were performed by using the RF module of COMSOL Multiphysics. The 2D simplified model was used to calculate the multilayer material field distribution of the microcavity device to reduce the computing load. For simplicity, the organic multilayer was assumed to be a single homogeneous organic layer, so the microcavity OLEFET is merged into the following parts: bottom/top mirror, electrode, dielectric layer, and organic layer (Fig. 1(b)). The refractive indices of the organic layer and dielectric layer are 1.75 and 1.53 [45,46], respectively. Optical constants for other materials used for simulation are from the software database. The

Optics EXPRESS

emission sources are treated as differently oriented point dipoles positioned at the corresponding emission interface. The simulated area is set to a lateral size of 12 μm around the dipole, and the entire structure is surrounded by a perfectly matching layer (PML) as the absorbing boundary condition to suppress any reflections at the boundaries.

**Funding.** National Natural Science Foundation of China (11904323); Research Funds of Zhengzhou University (32340305, 32410543).

**Disclosures.** The authors declare no conflicts of interest.

**Data availability.** Data underlying the results presented in this paper are not publicly available at this time but may be obtained from the authors upon reasonable request.

## References

1. F. Yin, J. B. De, M. H. Liu, H. Huang, H. Geng, J. N. Yao, Q. Liao, and H. B. Fu, "High-performance organic laser semiconductor enabling efficient light-emitting transistors and low-threshold microcavity lasers," Nano Lett. **22**(14), 5803–5809 (2022).
2. C. F. Liu, X. Liu, W. Y. Lai, and W. Huang, "Organic light-emitting field-effect transistors: Device geometries and fabrication techniques," Adv. Mater. **30**(52), 1802466 (2018).
3. S. Z. Bisri, T. Takenobu, and Y. Iwasa, "The pursuit of electrically-driven organic semiconductor lasers," J. Mater. Chem. C **2**(16), 2827–2836 (2014).
4. Y. Jiang, Y. Y. Liu, X. Liu, H. Lin, K. Gao, W. Y. Lai, and W. Huang, "Organic solid-state lasers: A materials view and future development," Chem. Soc. Rev. **49**(16), 5885–5944 (2020).
5. J. Zaumseil, "Recent developments and novel applications of thin film, light-emitting transistors," Adv. Funct. Mater. **30**(20), 1905269 (2020).
6. L. M. Kong, J. L. Wu, Y. G. Li, F. Cao, F. J. Wang, Q. Q. Wu, P. Y. Shen, C. X. Zhang, Y. Luo, L. Wang, L. Turyanska, X. W. Ding, J. H. Zhang, Y. B. Zhao, and X. Y. Yang, "Light-emitting field-effect transistors with EQE over 20% enabled by a dielectric-quantum dots-dielectric sandwich structure," Sci. Bull. **67**(5), 529–536 (2022).
7. Z. B. Wu, Y. Liu, E. J. Guo, G. Darbandy, S. J. Wang, R. Hubner, A. Kloes, H. Kleemann, and K. Leo, "Efficient and low-voltage vertical organic permeable base light-emitting transistors," Nat. Mater. **20**(7), 1007–1014 (2021).
8. M. Saliba, S. M. Wood, J. B. Patel, P. K. Nayak, J. Huang, J. A. Alexander-Webber, B. Wenger, S. D. Stranks, M. T. Horantner, J. T. W. Wang, R. J. Nicholas, L. M. Herz, M. B. Johnston, S. M. Morris, H. J. Snaith, and M. K. Riede, "Structured organic-inorganic perovskite toward a distributed feedback laser," Adv. Mater. **28**(5), 923–929 (2016).
9. V. G. Kozlov, G. Parthasarathy, P. E. Burrows, V. B. Khalfin, J. Wang, S. Y. Chou, and S. R. Forrest, "Structures for organic diode lasers and optical properties of organic semiconductors under intense optical and electrical excitations," IEEE J. Quantum Electron. **36**(1), 18–26 (2000).
10. F. Gourdon, M. Chakaroun, N. Fabre, J. Solard, E. Cambril, A. M. Yacomotti, S. Bouchoule, A. Fischer, and A. Boudrioua, "Optically pumped lasing from organic two-dimensional planar photonic crystal microcavity," Appl. Phys. Lett. **100**(21), 213304 (2012).
11. S. Z. Bisri, K. Sawabe, M. Imakawa, K. Maruyama, T. Yamao, S. Hotta, Y. Iwasa, and T. Takenobu, "Organic single-crystal light-emitting transistor coupling with optical feedback resonators," Sci. Rep. **2**(1), 985 (2012).
12. Y. Makino, A. Okada, S. Hotta, and T. Yamao, "Spectrally-narrowed emissions from organic transistors composed of layered crystals laminated on a two-dimensional diffraction grating (spectral narrowing from organic crystal transistors)," Mol. Cryst. Liq. Cryst. **566**(1), 8–12 (2012).
13. T. Yamao, Y. Sakurai, K. Terasaki, Y. Shimizu, H. Jinnai, and S. Hotta, "Current-injected spectrally-narrowed emissions from an organic transistor," Adv. Mater. **22**(33), 3708–3712 (2010).
14. Y. S. Hu, F. Bencheikh, S. Chenais, S. Forget, X. Y. Liu, and C. Adachi, "High performance planar microcavity organic semiconductor lasers based on thermally evaporated top distributed Bragg reflector," Appl. Phys. Lett. **117**(15), 153301 (2020).
15. Z. Z. Zhao, Y. Y. Xie, G. Z. Pan, P. N. Ni, Q. H. Wang, Y. B. Dong, L. C. Hu, J. Sun, H. D. Chen, C. Xu, and P. Genevet, "Dynamic phase manipulation of vertical-cavity surface-emitting lasers via on-chip integration of microfluidic channels," Opt. Express **29**(2), 1481–1491 (2021).
16. M. Taguchi, Y. Higase, and K. Yamashita, "Compact solid-state organic laser with fine and broadband wavelength tunability," Opt. Express **27**(24), 35548–35554 (2019).
17. S. B. Gorajoobi, G. S. Murugan, and M. N. Zervas, "Design of rare-earth-doped microbottle lasers," Opt. Express **26**(20), 26339–26354 (2018).
18. E. B. Namdas, B. Y. Hsu, J. D. Yuen, I. D. W. Samuel, and A. J. Heeger, "Optoelectronic gate dielectrics for high brightness and high-efficiency light-emitting transistors," Adv. Mater. **23**(20), 2353–2356 (2011).
19. M. C. Gwinner, D. Kabra, M. Roberts, T. J. K. Brenner, B. H. Wallikewitz, C. R. McNeill, R. H. Friend, and H. Sirringhaus, "Highly efficient single-layer polymer ambipolar light-emitting field-effect transistors," Adv. Mater. **24**(20), 2728–2734 (2012).
20. J. Lee, T. H. Han, M. H. Park, D. Y. Jung, J. Seo, H. K. Seo, H. Cho, E. Kim, J. Chung, S. Y. Choi, T. S. Kim, T. W. Lee, and S. Yoo, "Synergetic electrode architecture for efficient graphene-based flexible organic light-emitting diodes," Nat. Commun. **7**(1), 11791 (2016).

Optics EXPRESS


21. Y. S. Hu, J. Lin, L. Song, Q. P. Lu, W. B. Zhu, and X. Y. Liu, "Vertical microcavity organic light-emitting field-effect transistors," Sci. Rep. **6**(1), 23210 (2016).
22. L. Song, Y. S. Hu, N. Zhang, Y. T. Li, J. Lin, and X. Y. Liu, "Improved performance of organic light-emitting field-effect transistors by interfacial modification of hole-transport layer/emission layer: Incorporating organic heterojunctions," ACS Appl. Mater. Interfaces **8**(22), 14063–14070 (2016).
23. J. Lin, Y. S. Hu, and X. Y. Liu, "Microcavity-enhanced blue organic light-emitting diode for high-quality monochromatic light source with nonquarterwave structural design," Adv. Opt. Mater. **8**(7), 1901421 (2020).
24. E. F. Schubert, N. E. J. Hunt, M. Micovic, R. J. Malik, D. L. Sivco, A. Y. Cho, and G. J. Zydzik, "Highly efficient light-emitting-diodes with microcavities," Science **265**(5174), 943–945 (1994).
25. C. J. R. Sheppard, "Approximate calculation of the reflection coefficient from a stratified medium," Pure Appl. Opt. **4**(5), 665–669 (1995).
26. Y. J. Wan, J. Deng, W. L. Wu, J. D. Zhou, Q. Niu, H. Y. Li, H. K. Yu, C. Gu, and Y. G. Ma, "Efficient organic light-emitting transistors based on high-quality ambipolar single crystals," ACS Appl. Mater. Interfaces **12**(39), 43976–43983 (2020).
27. Z. S. Qin, H. K. Gao, J. Y. Liu, K. Zhou, J. Li, Y. Y. Dang, L. Huang, H. X. Deng, X. T. Zhang, H. L. Dong, and W. P. Hu, "High-efficiency single-component organic light-emitting transistors," Adv. Mater. **31**(37), 1903175 (2019).
28. R. Capelli, S. Toffanin, G. Generali, H. Usta, A. Facchetti, and M. Muccini, "Organic light-emitting transistors with an efficiency that outperforms the equivalent light-emitting diodes," Nat. Mater. **9**(6), 496–503 (2010).
29. L. Persano, A. Camposeo, P. Del Carro, E. Mele, R. Cingolani, and D. Pisignano, "Very high-quality distributed Bragg reflectors for organic lasing applications by reactive electron-beam deposition," Opt. Express **14**(5), 1951–1956 (2006).
30. J. Lin, X. Y. Guo, Y. Lv, X. Y. Liu, and Y. Wang, "Highly efficient microcavity organic light-emitting devices with narrow-band pure uv emission," ACS Appl. Mater. Interfaces **12**(9), 10717–10726 (2020).
31. M. S. Wang, J. Lin, Y. C. Hsiao, X. Y. Liu, and B. Hu, "Investigating underlying mechanism in spectral narrowing phenomenon induced by microcavity in organic light emitting diodes," Nat. Commun. **10**(1), 1614 (2019).
32. A. Genco, G. Giordano, S. Carallo, G. Accorsi, Y. Duan, S. Gambino, and M. Mazzeo, "High quality factor microcavity OLED employing metal-free electrically active Bragg mirrors," Org. Electron. **62**, 174–180 (2018).
33. M. Reufer, S. Riechel, J. M. Lupton, J. Feldmann, U. Lemmer, D. Schneider, T. Benstem, T. Dobbertin, W. Kowalsky, A. Gombert, K. Forberich, V. Wittwer, and U. Scherf, "Low-threshold polymeric distributed feedback lasers with metallic contacts," Appl. Phys. Lett. **84**(17), 3262–3264 (2004).
34. I. D. W. Samuel and G. A. Turnbull, "Organic semiconductor lasers," Chem. Rev. **107**(4), 1272–1295 (2007).
35. A. S. D. Sandanayaka, T. Matsushima, F. Bencheikh, S. Terakawa, W. J. Potscavage, C. J. Qin, T. Fujihara, K. Goushi, J. C. Ribierre, and C. Adachi, "Indication of current-injection lasing from an organic semiconductor," Appl. Phys. Express **12**(6), 061010 (2019).
36. H. F. Wittmann, J. Gruner, R. H. Friend, G. W. C. Spencer, S. C. Moratti, and A. B. Holmes, "Microcavity effect in a single-layer polymer light-emitting diode," Adv. Mater. **7**(6), 541–544 (1995).
37. U. Mescheder, I. Khazi, A. Kovacs, and A. Ivanov, "Tunable optical filters with wide wavelength range based on porous multilayers," Nanoscale Res. Lett. **9**(1), 427 (2014).
38. M. Chakaroun, A. Coens, N. Fabre, F. Gourdon, J. Solard, A. Fischer, A. Boudrioua, and C. C. Lee, "Optimal design of a microcavity organic laser device under electrical pumping," Opt. Express **19**(2), 493–505 (2011).
39. S. Chenais and S. Forget, "Recent advances in solid-state organic lasers," Polym. Int. **61**(3), 390–406 (2012).
40. W. Holzer, A. Penzkofer, and T. Tsuboi, "Absorption and emission spectroscopic characterization of $Ir(ppy)_3$," Chem. Phys. **308**(1-2), 93–102 (2005).
41. D. H. Kim, A. D'Aleo, X. K. Chen, A. D. S. Sandanayaka, D. D. Yao, L. Zhao, T. Komino, E. Zaborova, G. Canard, Y. Tsuchiya, E. Choi, J. W. Wu, F. Fages, J. L. Bredas, J. C. Ribierre, and C. Adachi, "High-efficiency electroluminescence and amplified spontaneous emission from a thermally activated delayed fluorescent near-infrared emitter," Nat. Photonics **12**(2), 98–104 (2018).
42. H. Nakanotani, T. Furukawa, T. Hosokai, T. Hatakeyama, and C. Adachi, "Light amplification in molecules exhibiting thermally activated delayed fluorescence," Adv. Opt. Mater. **5**(12), 1700051 (2017).
43. G. Zu, S. Li, J. P. He, H. H. Zhang, and H. B. Fu, "Amplified spontaneous emission from organic phosphorescence emitters," J. Phys. Chem. Lett. **13**(24), 5461–5467 (2022).
44. Z. Y. Yu, Y. S. Wu, L. Xiao, J. W. Chen, Q. Liao, J. N. Yao, and H. B. Fu, "Organic phosphorescence nanowire lasers," J. Am. Chem. Soc. **139**(18), 6376–6381 (2017).
45. Y. G. Li, M. Kovacic, J. Westphalen, S. Oswald, Z. F. May, C. Hanisch, P. A. Will, L. H. Jiang, M. Junghaehnel, R. Scholz, S. Lenk, and S. Reineke, "Tailor-made nanostructures bridging chaos and order for highly efficient white organic light-emitting diodes," Nat. Commun. **10**(1), 2972 (2019).
46. R. J. Xie, Z. Q. Li, E. D. Gu, S. L. Guo, and Y. Y. Yuan, "Absorption efficiency enhancement of organic solar cells by double grating structure," Photonics Nanostructures: Fundam. Appl. **38**, 100763 (2020).